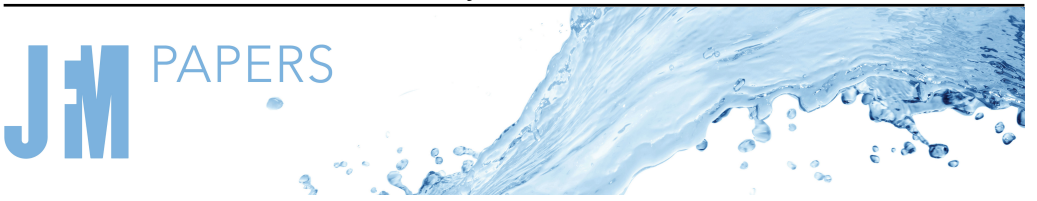
J. Fluid Mech. (2026), *vol.* 1043, A12, doi:10.1017/jfm.2026.12040



On the Poisson-source basis of logarithmic wall-pressure-variance growth

Jonathan Massey[1], **Joseph Klewicki**[2] and **Beverley McKeon**[1]

[1]Center for Turbulence Research, Stanford University, Stanford, CA 94305, USA

[2]Department of Mechanical Engineering, University of Melbourne, Parkville, VIC 3010, Australia

Corresponding author: Jonathan Massey, masseyj@stanford.edu

(Received 17 December 2025 UTC; revised 12 May 2026 UTC; accepted 13 August 2026 UTC)

In high-Reynolds-number wall-bounded flows, the inner-scaled wall-pressure variance is often represented as a logarithmic increase with frictional Reynolds number. We consider the two sources of the incompressible pressure–Poisson equation: a linear (rapid) term linked to mean shear and a nonlinear (slow) term composed of quadratic velocity fluctuations. This paper establishes a link between the sources and the coefficients in a logarithmic inner-scaled variance representation. To leading order we posit that the linear source provides a Reynolds-number-independent offset, while the nonlinear source contributes the logarithmic coefficient. The illustrative dataset is direct numerical simulation (DNS) at frictional Reynolds number $\delta^+ \approx 550$, although the principal contribution is the establishment of a mechanistic link to well-known high-δ^+ scalings of wall-bounded turbulence. Through consideration of the sources and the integral solution method of the Poisson equation, we find that the linear source contribution sits predominantly in the buffer layer and maps to the near-wall cycle. To leading order, this contribution becomes δ^+ invariant under inner scaling, thus contributing an offset in the logarithmic representation. The interfacial regions between uniform momentum zones characteristic of the inertial layer (vortical fissures) spatially localise strain and vorticity contributions and contain an increasingly large proportion of the strain and vorticity. We show that fissures act as a compact carrier for the source terms, with the nonlinear term especially prominent in these regions. By considering the inertial layer statistics, we link the changing nonlinear contribution to the $\ln \delta^+$ growth, in agreement with previous empirical observations.

Key words: turbulent boundary layers, hydrodynamic noise, turbulence theory

© The Author(s), 2026. Published by Cambridge University Press. This is an Open Access article, distributed under the terms of the Creative Commons Attribution licence (https://creativecommons.org/licenses/by/4.0/), which permits unrestricted re-use, distribution and reproduction, provided the original article is properly cited.

https://doi.org/10.1017/jfm.2026.12040 Published online by Cambridge University Press

1. Introduction

Wall-pressure fluctuations in turbulent wall-bounded flows underpin acoustic noise, structural fatigue and the performance of flow-control devices. In incompressible turbulence, the pressure satisfies a Poisson equation whose right-hand side contains two source terms: a linear (rapid) term coupling the mean shear to the fluctuating velocity field and a nonlinear (slow) term from quadratic velocity–velocity interactions; a viscous (Stokes) term arises from the Neumann boundary condition enforcing no slip at the wall. As the friction Reynolds number, $\delta^+ \equiv \delta u_\tau/\nu$, increases, the viscous contribution becomes progressively less important and the linear and nonlinear mechanisms dominate (Kim 1989; Jimenez & Hoyas 2008; Gerolymos *et al.* 2013). Here, δ is the boundary-layer (BL) thickness and half-height in the channel, u_τ is the friction velocity and ν is the kinematic viscosity.

Experiments and simulations have mapped the spectral and spatial origins of wall pressure: high frequencies are associated with the near-wall cycle, intermediate frequencies with the logarithmic region and low frequencies with the outer flow (Farabee & Casarella 1991; Gibeau & Ghaemi 2021; Dacome *et al.* 2025; Deshpande *et al.* 2026). Direct numerical simulation (DNS) at moderate δ^+ confirms that buffer layer eddies contribute strongly to both linear and nonlinear pressure, with viscous effects confined to the smallest scales (Kim 1989; Choi & Moin 1990; Chang *et al.* 1999; Hu *et al.* 2006; Lee & Moser 2015; Anantharamu & Mahesh 2020; Yang & Yang 2022). The wall-normal structure of the sources has been examined directly (Kim 1989; Anantharamu & Mahesh 2020). More broadly, wall-flow theory points to inner (viscous-scaled) and outer (boundary layer–scaled) regions (Bradshaw 1967; Panton *et al.* 2017; Deshpande *et al.* 2025), and suggests that pressure can be modelled as contributions from these separate regions. Figure 1(*a*) graphically depicts the procedure proposed by Massey *et al.* (2026*b*). Figure 1(*a*) describes the spectral structure of the wall pressure itself; no attribution of specific spectral features to $\mathcal{L}$ or $\mathcal{Q}$ is implied.

A key empirical observation, from high-δ^+ BLs and pipes (Klewicki *et al.* 2008; Fritsch *et al.* 2020, 2022; Dacome *et al.* 2025) as well as from DNS flows (Hoyas & Jiménez 2006; Schlatter & Örlü 2010; Lee & Moser 2015; Pirozzoli & Wei 2025), is the logarithmic growth of the inner-scaled wall-pressure variance, $\langle p_w^{+2}\rangle \propto \ln \delta^+$, where $p_w^+ \equiv p_w/(\rho u_\tau^2) \equiv p_w/\tau_w$ (figure 1*b*). Matched-asymptotic descriptions reproduce this growth (Panton *et al.* 2017), which is consistent with a progressive broadening of the low-wavenumber portion of the wall-pressure spectra. This finding suggests that the responsible physical processes are tied to the broadening of the log layer connecting the buffer and outer layer.

With homogeneous Neumann boundary conditions, the Green's function of the Poisson operator decays with wall-normal distance y and, in Fourier space, with the streamwise–spanwise wavenumber magnitude $k = \sqrt{k_x^2 + k_z^2}$. The ring-averaged representation is used only to expose the radial Green-function attenuation; the underlying wall-pressure and source fields remain anisotropic in (k_x, k_z). Throughout, we use (x, y, z) for the streamwise, wall-normal and spanwise coordinates, respectively. When tensor notation is convenient, repeated roman indices refer to components in this same Cartesian frame. Approximately, the Green's function decays proportionally to e^{-ky} (Anantharamu & Mahesh 2020); short-wavelength pressure fluctuations are supplied predominantly by near-wall source terms, whereas long-wavelength pressure is supplied by sources farther from the wall. This provides a bridge between wall-pressure statistics and the wall-normal distribution of the pressure sources. This non-local mapping motivates a relation between polar spectral content at the wall and the locations and types of Poisson sources across y.

https://doi.org/10.1017/jfm.2026.12040 Published online by Cambridge University Press

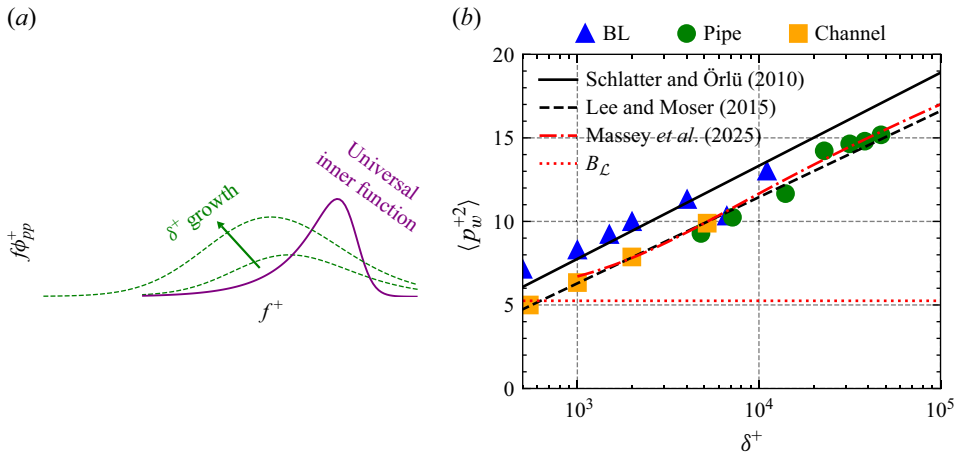


Figure 1. (*a*) Schematic of the wall-pressure spectra from Massey *et al.* (2026*b*), showing a universal – δ^+-independent – inner function and a δ^+-dependent outer function responsible for modelling the contribution from outer-scaled motions. The axes are omitted to illustrate this is a schematic, not a data plot. (*b*) $\langle p_w^{+2}\rangle$ for various DNS and experiments, showing the $\ln\delta^+$ growth. Blue triangles represent BL data from Fritsch *et al.* (2020, 2022), green circles represent pipe data from Dacome *et al.* (2025) and orange squares represent channel data from Lee & Moser (2015). The red dotted line is the variance from the universal inner function, showing that it contributes an $O(1)$ offset, $B_{\mathcal{L}}$, when the inner function is fully developed.

A growing body of theory, DNS and experimental work indicates that the inertial region organises into large uniform-momentum zones (UMZs) separated by narrow, locally sheet-like fissures bearing concentrated spanwise vorticity (Meinhart & Adrian 1995; Priyadarshana *et al.* 2007; De Silva *et al.* 2017; Heisel *et al.* 2022), in which enstrophy and strain are both large and strongly correlated. Very near the wall, vorticity is 2-D and space filling; it then undergoes stretching and tilting through the viscous and buffer layers. Vorticity in the inertial layer starts aligning in the streamwise direction under the action of mean shear and concentrates within thin vortical fissures. In this UMZ–vortical-fissure picture, the fissure thickness, when scaled by outer length, decreases approximately as $1/\sqrt{\delta^+}$, while the streamwise velocity jump across a fissure is $O(u_\tau)$; both are central empirical inputs in minimal models that reproduce turbulent statistics at high δ^+ (Bautista *et al.* 2019). Theoretical analyses of the mean momentum equation further support the view that with increasing δ^+, an increasing fraction of the vorticity outside the buffer region is confined within such narrow fissures that disperse across a hierarchy of wall-normal layers (Klewicki 2013; Morrill-Winter & Klewicki 2013).

At high δ^+ incompressible wall turbulence, the wall-pressure variance is often represented by

$$\langle p_w^{+2}\rangle = B_{\mathcal{L}} + A_{\mathcal{Q}}\ \ln\delta^+. \tag{1.1}$$

Empirical fits give, for example, $\langle p_w^{+2}\rangle = 2.42\ln\delta^+ - 8.96$ for BL data (Schlatter & Örlü 2010) and $\langle p_w^{+2}\rangle = 2.24\ln\delta^+ - 9.18$ for channel-flow data (Lee & Moser 2015). We stress that (1.1) is adopted here as a working asymptotic hypothesis, motivated by the currently available wall-pressure data, rather than as an uncontested starting point. More broadly, the existence and universality of logarithmic overlap laws for fluctuation statistics in wall turbulence remain debated, and alternative bounded or quarter-power forms have been proposed from both asymptotic and symmetry-based perspectives (Oberlack *et al.* 2022; Hoyas *et al.* 2022; Chen & Sreenivasan 2023). In particular, Chen & Sreenivasan

https://doi.org/10.1017/jfm.2026.12040 Published online by Cambridge University Press

(2023) argue for a bounded outer form for several wall-bounded fluctuation quantities, including the root-mean-square (r.m.s.) pressure, while Nagib *et al.* (2024) revisit the logarithmic-versus-quarter-power interpretation for normal stresses using indicator functions applied to computational data. The present paper does not attempt to resolve that broader debate. Instead, conditional on the empirical wall-pressure form in (1.1), we ask what Poisson-source mechanisms would be consistent with such behaviour and what that implies for the coefficients $B_{\mathcal{L}}$ and $A_{\mathcal{Q}}$.

In this paper, we provide evidence to support the link between (1.1) and the processes governing the behaviour of the Poisson sources themselves. Using channel DNS at $\delta^+ \approx 550$, we show that the elliptic attenuation of the Green's function maps contributions from the source at $yk \approx O(1)$. The r.m.s. of the source terms shows that the linear source peaks in the buffer layer, while the nonlinear source is made up of a balance of strain and enstrophy peaking in the inertial layer. Next, we show that the linear source – to leading order – is tied to the near-wall cycle and asymptotes with δ^+ to an $O(1)$ offset to the logarithmic $\langle p_w^{+2} \rangle$ growth, arising as $B_{\mathcal{L}}$ in (1.1). Finally, we show that inertial layer fissures act as compact carriers of the nonlinear source that contributes to $A_{\mathcal{Q}} \ln \delta^+$. This connection of the nonlinear source to inertial layer processes, and thus statistics, provides a mechanistic link between the nonlinear source and the $\ln \delta^+$ growth of $\langle p_w^{+2} \rangle$. Because the detailed source decomposition is available only at $\delta^+ \approx 550$, these proposed δ^+ trends are necessarily inferential: they combine the single-Reynolds-number DNS with prior high-Reynolds-number evidence and scaling arguments, and therefore should be read as hypotheses about the asymptotic regime rather than as a direct verification of generality. Nevertheless, we regard this case as adequate for mechanistic illustration, the viscous contribution is already subdominant, and the source-localisation and wall-mapping mechanisms are directly visible in the decomposed fields. Finally, we use our simplifying assumptions to predict $A_{\mathcal{Q}} \approx 2$, in good agreement with previous empirical observations.

2. Components of the pressure Poisson equation

Following Mansour *et al.* (1988) and Kim (1989), and using the Einstein summation convention where roman indices are just component indices in that same Cartesian frame, the fluctuating pressure satisfies

$$\partial_i \partial_i p = \underbrace{-2 \frac{\mathrm{d}U}{\mathrm{d}y} \partial_x v}_{\textit{linear } (\mathcal{L})} + \underbrace{-\partial_j \partial_k \left(u_j u_k\right)}_{\textit{nonlinear } (\mathcal{Q})} + \overline{\partial_j \partial_k \left(u_j u_k\right)}, \tag{2.1}$$

where $\tilde{u}_i = U_i + u_i$. In the resolvent analysis framework (McKeon & Sharma 2010), $\mathcal{Q}$ is the dilatational part of the nonlinear forcing to the linearised Navier–Stokes operator, namely the gradient of the Reynolds stress tensor (Rosenberg & McKeon 2019; Blanco *et al.* 2024). Rewritten in vorticity/strain form by considering the symmetric and antisymmetric parts of the Reynolds stress gradient tensor (Bradshaw & Koh 1981), the equation reads

$$\partial_i \partial_i p = \underbrace{2 \Omega_z \partial_x v}_{\mathcal{L}} + \underbrace{\left(\overbrace{\frac{1}{2} \omega_i \omega_i}^{\mathcal{T}} - \overbrace{S_{ij} S_{ij}}^{\mathcal{S}} \right) - \overline{\left(\frac{1}{2} \omega_i \omega_i - S_{ij} S_{ij} \right)}}_{\mathcal{Q}}, \tag{2.2}$$

https://doi.org/10.1017/jfm.2026.12040 Published online by Cambridge University Press

where

$$S_{ij} = \frac{1}{2}(\partial_i u_j + \partial_j u_i), \qquad \omega_i = \varepsilon_{ijk}\,\partial_j u_k, \qquad \Omega_z = -\frac{\mathrm{d}U}{\mathrm{d}y}\,, \tag{2.3}$$

with $\mathcal{Q} = \mathcal{T} - \mathcal{S}$.
We define the pressure components by

$$\partial_i \partial_i p_{\mathcal{L}} = \mathcal{L}, \qquad (\partial_y p_{\mathcal{L}})\big|_{y=\pm 1} = 0, \tag{2.4a}$$

$$\partial_i \partial_i p_{\mathcal{Q}} = \mathcal{Q}, \qquad (\partial_y p_{\mathcal{Q}})\big|_{y=\pm 1} = 0, \tag{2.4b}$$

$$\partial_i \partial_i p_{\nu} = 0, \qquad (\partial_y p_{\nu})\big|_{y=\pm 1} = Re^{-1}\,\partial_j \partial_j v\,, \tag{2.4c}$$

with $Re \equiv \delta U_e/\nu$, and U_e is the centreline/edge velocity in the channel/BL. It follows that

$$p = p_{\mathcal{L}} + p_{\mathcal{Q}} + p_{\nu}\,, \tag{2.5}$$

where $p_{\mathcal{L}}$, $p_{\mathcal{Q}}$ and p_{ν} are the linear, nonlinear and viscous components of the pressure, respectively.

Because the analysis below is restricted to $k = \sqrt{k_x^2 + k_z^2} > 0$, the wall-parallel mean $\overline{\mathcal{Q}}(y)$ contributes only to the $(k_x, k_z) = (0, 0)$ mode and therefore does not appear explicitly in the Fourier-space expressions below.

Let $\widehat{\cdot}$ denote the (k_x, k_z) Fourier transform and $k = \sqrt{k_x^2 + k_z^2} > 0$. In a channel $y \in [-1, 1]$ with homogeneous Neumann boundary conditions, the solution of (2.1) for the linear and nonlinear sources $\mathcal{M} \in \{\mathcal{L}, \mathcal{Q}\}$ admits the integral representation

$$\widehat{p}_{\mathcal{M}}(k, y; \delta^+) = \int_{-1}^{1} g(k;\ y, y')\,\widehat{\mathcal{M}}(y', k; \delta^+)\,\mathrm{d}y'\,, \tag{2.6a}$$

$$g(k;\ y, y') = -\frac{\cosh\big(k(1 - y_>)\big)\ \cosh\big(k(1 + y_<)\big)}{k\ \sinh(2k)}\,, \tag{2.6b}$$

with $y_< = \min(y, y')$ and $y_> = \max(y, y')$, where $y' \in [-1, 1]$ is the source-point integration variable. The viscous component p_ν is obtained through enforcement of no slip via the Neumann boundary condition.

Evaluating (2.6) at either wall yields a convolution between the sources and a single-wall kernel. For the bottom wall ($y = -1$),

$$\widehat{p}_{\mathcal{M},w^-}(k; \delta^+) = \int_{-1}^{1} G^-(k, y')\,\widehat{\mathcal{M}}(y', k; \delta^+)\,\mathrm{d}y', \quad G^-(k, y') = -\frac{1}{k}\,\frac{\cosh\big(k(1 - y')\big)}{\sinh(2k)}, \tag{2.7a}$$

and top wall ($y = +1$),

$$\widehat{p}_{\mathcal{M},w^+}(k; \delta^+) = \int_{-1}^{1} G^+(k, y')\,\widehat{\mathcal{M}}(y', k; \delta^+)\,\mathrm{d}y', \quad G^+(k, y') = -\frac{1}{k}\,\frac{\cosh\big(k(1 + y')\big)}{\sinh(2k)}. \tag{2.7b}$$

For later convenience, we define the inner-scaled distances from the bottom and top walls as

$$y_-^+ \equiv \delta^+(1 + y), \qquad y_+^+ \equiv \delta^+(1 - y), \tag{2.8}$$

or, equivalently, $y_\pm^+ \equiv \delta^+(1 \mp y)$.

https://doi.org/10.1017/jfm.2026.12040 Published online by Cambridge University Press

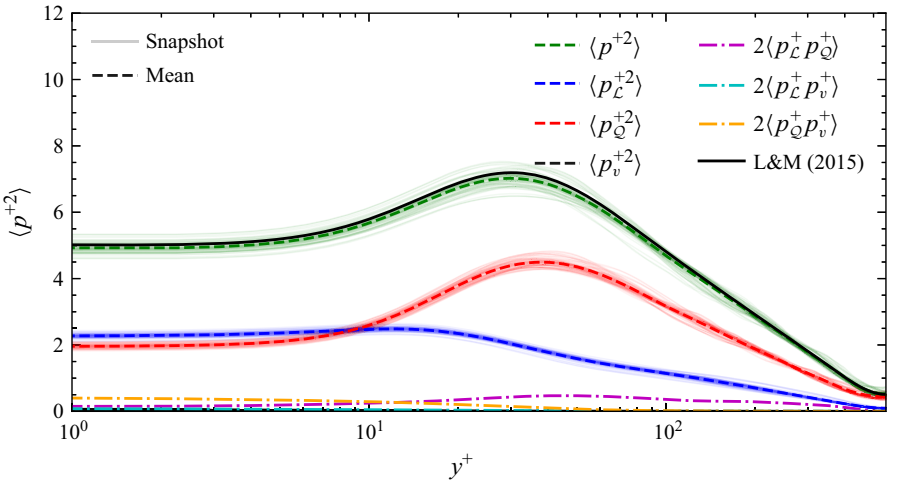


Figure 2. Instantaneous and mean r.m.s. profiles of the pressure across a half-channel width at $\delta^+ \approx 550$ and a comparison to the r.m.s. reported by Lee & Moser (2015). The linear, nonlinear and viscous contributions to the variance as well as the cross terms are shown. Light curves indicate instantaneous profiles, while the darker/dashed curves indicate the corresponding mean profiles.

Writing the hyperbolic functions in exponential form makes the wall-normal attenuation explicit,

$$G^{-}(k,\, y') = -\frac{1}{k}\frac{\mathrm{e}^{-k(1+y')} + \mathrm{e}^{-k(3-y')}}{1-\mathrm{e}^{-4k}} \xrightarrow[k\gg 1]{} -\frac{1}{k}\mathrm{e}^{-k(1+y')}, \tag{2.9}$$

so that each Fourier mode decays exponentially with the wall-normal distance from the source to the wall. Equivalently, the full-field kernel in (2.6) has the leading-order form

$$g(k;\, y,\, y') \sim -\frac{1}{2k}\mathrm{e}^{-k|y-y'|}, \tag{2.10}$$

demonstrating the expected elliptic attenuation: contributions at wavenumber k are exponentially suppressed away from their source with characteristic scale $1/k$. Below, we focus on the wall pressure and its decomposition,

$$p_w = (p_{\mathcal{L}})_w + (p_{\mathcal{Q}})_w + (p_v)_w, \tag{2.11}$$

with each component obtained by substituting $\widehat{\mathcal{M}}$ into (2.7), and we drop the $\cdot_w$ subscript for brevity. In the bottom-wall attribution maps below, y denotes source distance from that wall, so $G(k,\, y)$ denotes the corresponding single-wall kernel; for $k \gg 1$, $G(k,\, y) \sim -k^{-1}\mathrm{e}^{-ky}$.

The dataset used derives from a previously published channel-flow DNS at $\delta^+ \approx 550$ (Huang *et al.* 2026) that employs the method of Flores & Jiménez (2006). Figure 2 shows a comparison with results from Lee & Moser (2015) (as reported in Panton *et al.* (2017)) and confirms that we match $\langle p^2\rangle^+$ at comparable δ^+. Figure 2 shows that this case lies close to the DNS of Lee & Moser (2015) and that the viscous contribution is already small compared with the linear and nonlinear terms, as noted by Kim (1989) and Jimenez & Hoyas (2008). We use $\delta^+ \approx 550$ as an illustrative dataset: it is not sufficient to settle asymptotic scaling, but it is sufficient to expose the source localisation and wall-mapping mechanisms on which the present interpretation rests. The nonlinear pressure variance is comparable with or larger than the linear contribution everywhere except very near the wall, with the mean-square nonlinear source peaking near $y^+ \approx 20$, in line with previous

https://doi.org/10.1017/jfm.2026.12040 Published online by Cambridge University Press

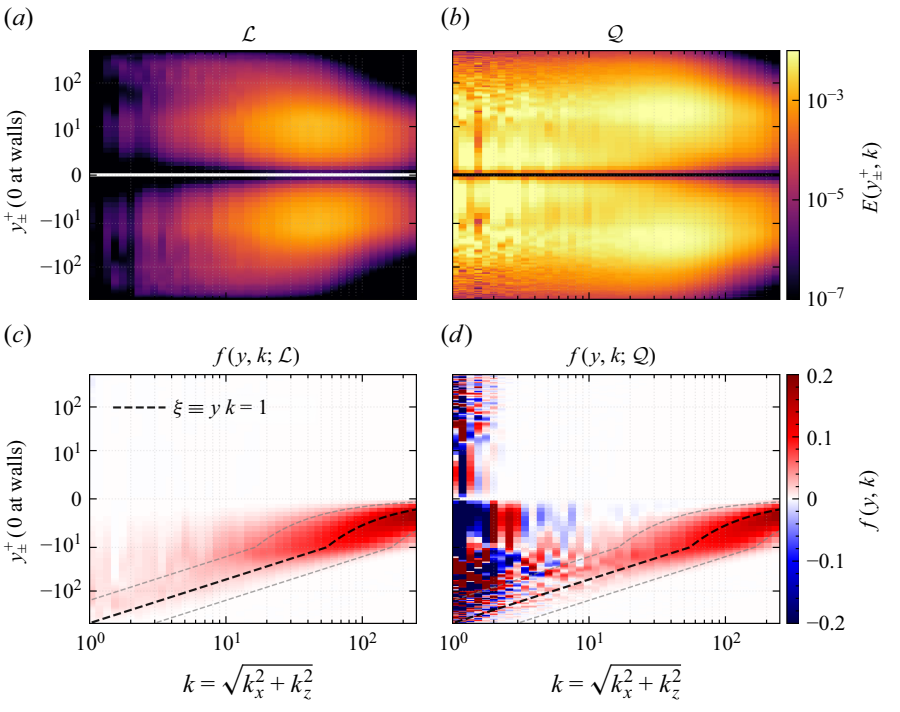


Figure 3. Ring-averaged y^+–k spectra of (*a*) linear $\mathcal{L}$ and (*b*) nonlinear $\mathcal{Q}$ sources, as well as the corresponding wall-pressure attribution maps to the bottom wall for (*c*) linear pressure and (*d*) nonlinear pressure. (*c*, *d*) The black dashed line indicates $k\,y = 1$, and the two grey lines indicate $\xi = 0.3$ and $\xi = 3$. The kink in the lines is due to the change from log to linear scaling at $y^+ = 10$ toward the channel wall.

work (Kim 1989; Panton *et al.* 2017; Yang & Yang 2022). The cross terms contributing to the variance are also shown. Although Yang & Yang (2022) show that such cross terms can contribute significantly, in the present case they remain smaller than the dominant linear and nonlinear self-contributions. We therefore focus below on the mechanisms associated with $\mathcal{L}$ and $\mathcal{Q}$.

3. Source-term structure

The structure of the source terms is illustrated in figure 3. Figure 3(*a*) shows that the $\mathcal{L}$ energy is concentrated near $y^+ \approx 10$ and at relatively high k, whereas figure 3(*b*) shows that $\mathcal{Q}$ peaks farther out ($y^+ \approx 20$) and extends to the highest resolved k. As (2.2) shows, $\mathcal{Q}$ is the difference of two large, correlated quadratic forms. Strong cancellations occur when it is mapped onto the wall, which makes it susceptible to sign changes and partial cancellation. When mapped to the wall, this yields the positive and negative attribution regions seen in figure 3(*d*).

3.1. *Variance attribution*

Figures 3(*c*) and 3(*d*) highlight how the source terms are mapped to the wall-pressure fluctuations by showing the instantaneous wall-pressure attribution maps for $\mathcal{L}$ and $\mathcal{Q}$. Here, consistent with the bottom-wall maps, y denotes source distance from the bottom wall. The attribution is defined as the signed fractional contribution of sources at distance y to the wall-pressure mode at wavenumber k. We define the attribution function $f(y, k)$ as

https://doi.org/10.1017/jfm.2026.12040 Published online by Cambridge University Press

$$f(y,k)=\frac{\mathrm{Re}\{G(k,y)\,\widehat{\mathcal{M}}(y,k)\,\widehat{p}^{*}(k)\}}{|\widehat{p}(k)|^{2}}\,, \tag{3.1}$$

where Re denotes the real part. For each k, $\int_0^2 f(y,k)\,\mathrm{d}y=1$; positive values indicate contributions that are in phase with the wall-pressure mode, whereas negative values indicate cancellation. Figure 3(*c*) shows that the attribution associated with $\mathcal{L}$ is positive everywhere. For $k\lesssim 10$ it is distributed over a range of wall-normal distances, whereas with increasing k it becomes concentrated over a narrower band. The attribution associated with $\mathcal{Q}$ in figure 3(*d*) is similar for $k\gtrsim 10$. For $k\lesssim 10$, however, the nonlinear map develops alternating positive and negative regions, indicating that the wall-pressure mode is assembled through partial cancellation among source layers, including appreciable contributions from both sides of the channel centreline.

3.2. *Elliptic attenuation*

Heuristically, the elliptic attenuation reflects the balance between the algebraic spectral decay of the source and the exponential decay of the Green's kernel with wall-normal distance. For a wall-parallel wavenumber magnitude k at height y, the wall-weighted amplitude scales as

$$|G(k,y)\,\widehat{\mathcal{M}}(y,k)|\sim\frac{\mathrm{e}^{-ky}}{k}\times\big[\text{algebraic source decay in }k\big], \tag{3.2}$$

where the factor e^{-ky} comes from the Green's kernel for $k\gg 1$ (2.9), so that contributions from a layer at y are rapidly attenuated once $k\,y\gg 1$. Accordingly, we use this simplifying assumption to define the effective envelope of wall-source communication by a fixed iso-attenuation criterion on the kernel; for instance,

$$\mathrm{e}^{-ky}=\mathrm{e}^{-1}\quad\Longleftrightarrow\quad\xi\equiv k\,y=1, \tag{3.3}$$

where $\xi=\mathcal{O}(1)$ denotes one e-fold of attenuation. For $\xi\ll 1$, the kernel hardly filters (and the communication to the wall is then controlled by the source spectrum), whereas for $\xi\gg 1$, the exponential damping dominates and suppresses the contribution. The line $\xi=1$ therefore serves as a practical elliptic attenuation boundary in (k,y)-space.

Figures 3(*c*) and 3(*d*) plot the $\xi=1$ line as an approximate envelope: high-k contributions from a given layer lie predominantly on or slightly above this curve, while the low-k contributions ($k\lesssim 10$) extend more broadly, with $\xi=1$ providing an upper bound on their influence. This low-k behaviour is influenced by channel-specific effects, in particular the cancellation of contributions across the centreline and the relative (to zero pressure gradient BL flows) suppression of the largest scales. To keep the theoretical picture consistent with single-wall geometries, we therefore focus, for the present envelope argument, on the region $k>10$, and reiterate that the e^{-ky} decay used in (2.9) is the large-k ($k\gg 1$) asymptotic form of the Green's kernel. Figures 3(*c*) and 3(*d*) also plot lines at $\xi=0.3$ and $\xi=3$ to give a sense of the $O(1)$ range of the elliptic attenuation.

3.3. *Positive and negative* $\mathcal{Q}$

It is useful to distinguish the local enstrophy–strain imbalance,

$$\mathcal{B}\equiv\mathcal{T}-\mathcal{S}, \tag{3.4}$$

from the nonlinear Poisson source,

$$\mathcal{Q}=\mathcal{B}-\overline{\mathcal{B}}. \tag{3.5}$$

https://doi.org/10.1017/jfm.2026.12040 Published online by Cambridge University Press

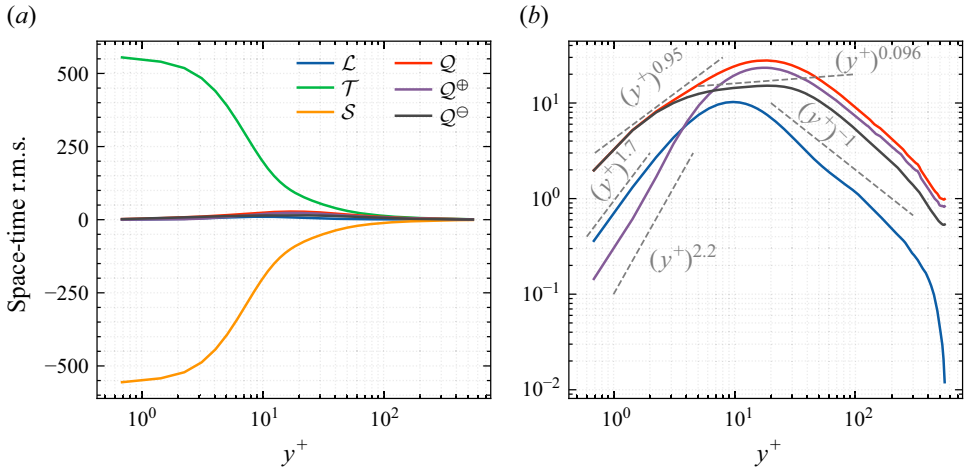


Figure 4. Profiles of the r.m.s. of the Poisson source components versus y^+. (*a*) The individual components, $\mathcal{L}$, $\mathcal{T}$, $-\mathcal{S}$ and $\mathcal{Q}$, and the sign-split parts, $\mathcal{Q}^{\oplus}$ and $\mathcal{Q}^{\ominus}$ ((2.1), (2.2) and (3.6)). (*b*) Log–log view of selected curves.

Regions with $\mathcal{B} > 0$ are locally enstrophy-dominated, whereas regions with $\mathcal{B} < 0$ are locally strain-dominated. By contrast, the sign of $\mathcal{Q}$ indicates whether the local enstrophy–strain imbalance lies above or below its mean, not simply whether $\mathcal{T}$ is larger or smaller than $\mathcal{S}$. Thus, $\mathcal{Q} > 0$ and $\mathcal{Q} < 0$ identify positive and negative nonlinear source events, respectively.

To isolate these two classes of events, we define

$$\mathcal{Q}^{\oplus} = \max(\mathcal{Q}, 0), \qquad \mathcal{Q}^{\ominus} = \max(-\mathcal{Q}, 0), \tag{3.6}$$

and examine their r.m.s. profiles separately.

3.4. *Root mean square of the source components*

Profiles of the r.m.s. of the Poisson-source terms versus y^+ quantify the available source amplitude prior to cancellation by sign and by Green-function weighting. Figure 4(*a*) shows that $\mathcal{T}$ and $\mathcal{S}$ are individually much larger than $\mathcal{L}$ and $\mathcal{Q}$, so that the nonlinear source arises from a strong cancellation between large enstrophy and strain contributions. Figure 4(*b*) shows the selected r.m.s. profiles on logarithmic axes. The linear source $\mathcal{L}$ peaks at $y^+ \approx 10$, whereas $\mathcal{Q}$ peaks farther from the wall, at $y^+ \approx 15$–20, and remains larger than $\mathcal{L}$ over most of the domain. Over the inertial layer, both $\mathcal{L}$ and $\mathcal{Q}$ decay approximately as y^{+-1}.

The $\mathcal{Q}^{\oplus}/\mathcal{Q}^{\ominus}$ split isolates positive and negative nonlinear source events, rather than enstrophy- and strain-dominated events. Very near the wall, $\mathcal{Q}^{\ominus}_{rms} > \mathcal{Q}^{\oplus}_{rms}$. Beyond $y^+ \approx 7$, $\mathcal{Q}^{\oplus}_{rms}$ rises rapidly and becomes comparable to, and near the peak slightly larger than, $\mathcal{Q}^{\ominus}_{rms}$; farther from the wall the two remain of the same order.

4. Direct source density of the linear contribution

The δ^+-invariant inner function of the wall-pressure spectrum modelled by Massey *et al.* (2026*b*) is defined only once δ^+ is sufficiently large. In practice, the proposed $B_{\mathcal{L}}$ offset in (1.1) is the asymptotic value obtained when that inner contribution is integrated to $\langle p^{+2} \rangle$. The question is therefore whether the linear self-contribution can generate a logarithmic dependence as the wall-normal domain expands with δ^+.

https://doi.org/10.1017/jfm.2026.12040 Published online by Cambridge University Press

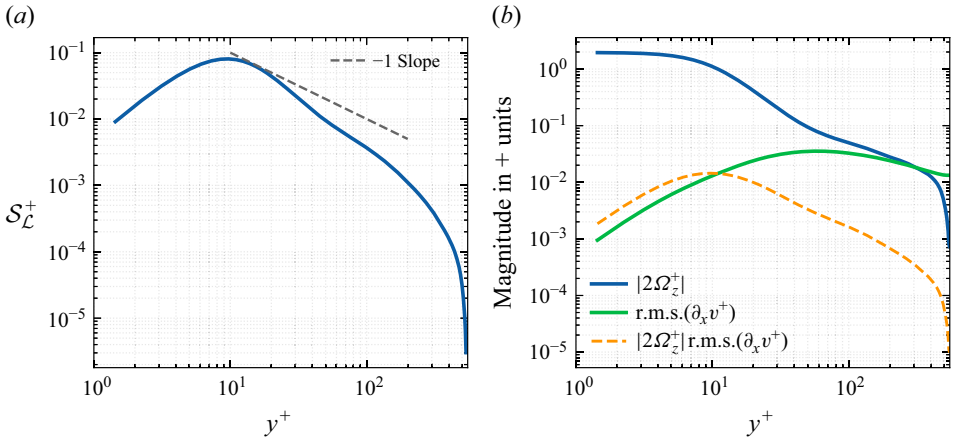


Figure 5. Linear-source variance-density decomposition at $\delta^+ \approx 550$. (*a*) Direct signed wall-normal source density of the linear pressure variance, $\mathcal{S}^+_{\mathcal{L}}(y^+)$, defined by (4.2); the solid curve shows the positive part and the dotted curve shows the magnitude of the negative part. (*b*) Inner-scaled magnitudes of the two local factors entering $\mathcal{L}$: $|2\Omega^+_z|$, r.m.s.$(\partial_{x^+} v^+)$, and their pointwise product. Comparing (*a*) and (*b*) distinguishes local source amplitude from the Green-function-weighted, phase-aware contribution to wall-pressure variance.

The r.m.s. profiles discussed above quantify the amplitude available before wall mapping. Figure 5(*b*) shows that the local product $|2\Omega^+_z|\,\mathrm{r.m.s.}(\partial_{x^+} v^+)$ is weighted toward the near-wall region. This is suggestive, but not sufficient: it does not include the Green-function weighting, wall-normal correlations orcancellations between source layers.

A direct test is obtained from the wall-normal source density of the variance. For a source component $\mathcal{M} \in \{\mathcal{L}, \mathcal{Q}\}$, multiplying (2.7) by $\widehat{p}^*_{\mathcal{M}}$, summing over wall-parallel Fourier modes, and averaging gives

$$\langle p^2_{\mathcal{M}} \rangle = \int_{-1}^{1} \mathcal{S}_{\mathcal{M}}(y)\,\mathrm{d}y, \tag{4.1}$$

with the signed wall-normal source density

$$\mathcal{S}_{\mathcal{M}}(y) = \sum_{\boldsymbol{k}} \mathrm{Re}\left\{ G_w(k, y)\left\langle \widehat{\mathcal{M}}(\boldsymbol{k}, y)\,\widehat{p}^*_{\mathcal{M}}(\boldsymbol{k}) \right\rangle \right\}. \tag{4.2}$$

Equivalently,

$$\mathcal{S}_{\mathcal{M}}(y) = \int_{-1}^{1} \sum_{\boldsymbol{k}} G_w(k, y) G_w(k, y')\mathrm{Re}\left\{ \left\langle \widehat{\mathcal{M}}(\boldsymbol{k}, y)\widehat{\mathcal{M}}^*(\boldsymbol{k}, y') \right\rangle \right\} \mathrm{d}y'. \tag{4.3}$$

These expressions retain the Green-function weighting, wall-normal correlations and phase cancellations omitted by r.m.s.$(\mathcal{M})$. The plus-normalised density is defined so that $\mathcal{S}^+_{\mathcal{M}}(y^+)\,\mathrm{d}y^+$ contributes to $\langle p^{+2}_{\mathcal{M}} \rangle$.

Figure 5(*a*) shows the resulting $\mathcal{S}^+_{\mathcal{L}}(y^+)$. The density rises through the viscous and buffer layers, peaks at near-wall distances and then decays through the logarithmic and outer regions more rapidly than the $(y^+)^{-1}$ guide. The negative part of the signed density is small and does not form a compensating outer contribution.

This observation is most naturally interpreted as a statement about the possible asymptotic contribution. If, over an inertial range $y^+_0 \ll y^+ \ll \delta^+$, the density were Reynolds-number invariant in inner units, then a non-cancelling $\mathcal{S}^+_{\mathcal{L}} \sim C/y^+$ tail would

https://doi.org/10.1017/jfm.2026.12040 Published online by Cambridge University Press

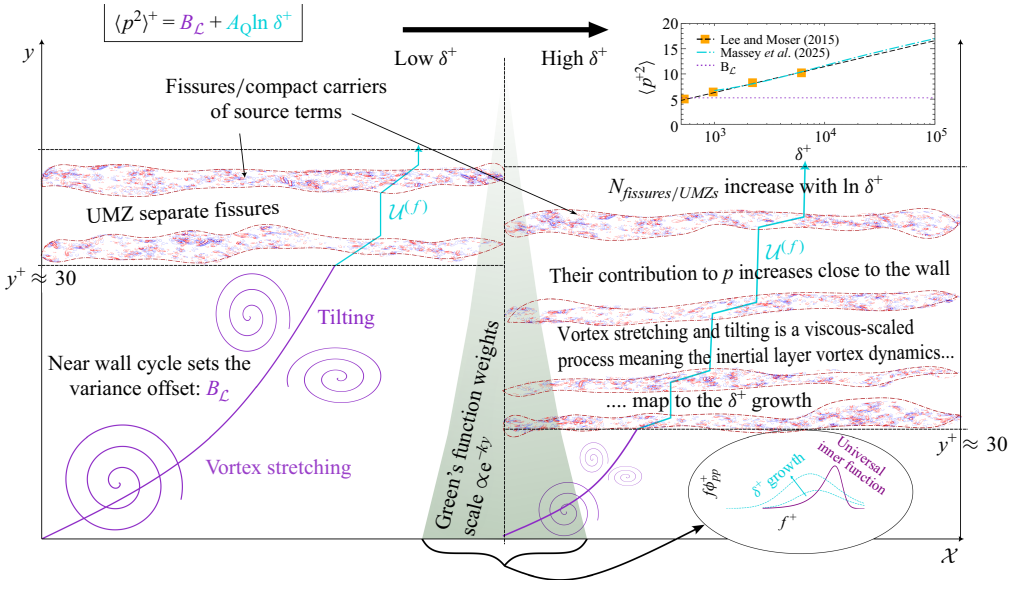


Figure 6. Schematic of the physical process that yields the $\ln \delta^+$ growth of $\langle p^{+2}\rangle$. Vortex stretching/tilting produces thin, sheet-like fissures that carry the Poisson sources compactly across the inertial layer and imprint at the wall through an elliptic Green's mapping that favours low wall-parallel wavenumbers.

produce a contribution $C \ln(\delta^+/y_0^+)$ as δ^+ increases. Any steeper decay leads instead to a contribution that approaches a constant as the upper limit extends. The measured $\mathcal{S}_\mathcal{L}^+$ in figure 5(*a*) is consistent with the latter behaviour.

The key point is therefore that the variance density, not the local amplitude, determines the Reynolds-number dependence. The difference between panels (*a*) and (*b*) highlights this: the local product $|2\Omega_z^+|$ r.m.s.$(\partial_{x^+} v^+)$ does not account for Green-function weighting or cancellation and does not predict the decay of $\mathcal{S}_\mathcal{L}^+$.

The conclusion from this section is necessarily limited. The $\delta^+ \approx 550$ dataset does not establish the asymptotic Reynolds-number decomposition of $\langle p^{+2}\rangle$. It does show that, in the present flow, the exact self-source density of $\langle p_\mathcal{L}^{+2}\rangle$ is near-wall dominated and decays more rapidly than the form required to produce a logarithmic contribution. This is consistent with interpreting $B_\mathcal{L}$ as a predominantly inner-set contribution, while any $\ln \delta^+$ growth of the total variance arises from components whose source densities do not decay with the expanding of the inertial layer. Subsequent work explores this conclusion more concretely (Massey *et al.* 2026*a*). The next section considers this possibility for $\mathcal{Q}$.

5. Fissures as compact carriers of the source terms

Moving away from the mid-δ^+ dataset, we aim to describe the mechanistic link between the pressure-Poisson sources and the vortical-fissure picture of the inertial layer. The theoretical arguments presented rest on the compact spatial support of the sources within the fissures. We define compact support as regions where the source terms are significantly non-zero and spatially localised. Figure 6 summarises the formation and alignment of these fissures and their variation with δ^+. We consider a single fissure neighbourhood and introduce local coordinates

$$(s, n, t) = (x, y, z) + O(\theta), \qquad \theta \ll 1, \tag{5.1}$$

https://doi.org/10.1017/jfm.2026.12040 Published online by Cambridge University Press

with s (approximately streamwise), n (approximately wall-normal) and t (approximately spanwise) (Cui & Jacobi 2025). In the fissure frame, the velocity is decomposed into a fissure-aligned (skeletal) probabilistic mean (Bautista *et al.* 2019) and residuals,

$$\tilde{u}^{(f)}(s,n,t) = \mathcal{U}^{(f)}(n) + u^{(f)}(s,n,t) \approx \mathcal{U}^{(f)}(y) + u^{(f)}(x,y,z), \tag{5.2a}$$

$$\tilde{v}^{(f)}(s,n,t) = v^{(f)}(s,n,t) \approx v^{(f)}(x,y,z), \tag{5.2b}$$

$$\tilde{w}^{(f)}(s,n,t) = w^{(f)}(s,n,t) \approx w^{(f)}(x,y,z), \tag{5.2c}$$

where $\mathcal{U}^{(f)}$ is the fissure-aligned most probable (UMZ-like) streamwise profile and $u^{(f)}$, $v^{(f)}$ and $w^{(f)}$ are zero mean under a fissure-aligned conditional average, $\langle (u_i)^{(f)} \rangle_f = 0$. The global mean remains $U_i = (U(y), 0, 0)$. Consistent with the UMZ–vortical-fissure picture, the skeletal profile is a near step with jump $\Delta\mathcal{U}^{(f)} = O(u_\tau)$ across thickness $\delta^{(f)}$, such that

$$\partial_y \mathcal{U}^{(f)} \sim \frac{\Delta \mathcal{U}^{(f)}}{\delta^{(f)}} \approx \frac{u_\tau}{\delta^{(f)}} \quad \text{with} \quad \delta^{(f)} \ll \ell_{s,t}. \tag{5.3}$$

This yields the local velocity gradient

$$\partial_i \tilde{u}_j^{(f)} \approx \underbrace{\begin{pmatrix} 0 & 0 & 0 \\ \partial_y \mathcal{U}^{(f)} & 0 & 0 \\ 0 & 0 & 0 \end{pmatrix}}_{\textit{mean fissure shear}} + \partial_i u_j^{(f)}. \tag{5.4}$$

Before turning to the spectral content of the source decomposition that follows, we emphasise that k throughout this section refers to the wall-parallel wavenumber magnitude entering the Green's function in (2.7). The wall-normal thinness of a fissure (its small $\delta^{(f)}$) does not enter this Fourier decomposition; what matters for wall transmission is the source's footprint in the wall-parallel (x, z) plane. A fissure is thin in y but coherent over along-fissure scales $\ell_{s,t} \gg \delta^{(f)}$, so its wall-parallel spectrum is concentrated at relatively low k even though the source amplitude within the fissure is large and locally sheet-like.

To expose compact support of the nonlinear source $\mathcal{Q} = -\partial_i \partial_j (u_i u_j)$ in local coordinates, we write the fluctuations as the sum of a skeletal contribution (support confined to the fissure) and residuals that are zero mean in the fissure frame,

$$u_i \approx \underbrace{\left(\mathcal{U}^{(f)} - U\right)}_{U^{(sk)}(y)} + \underbrace{\left(u^{(f)}, v^{(f)}, w^{(f)}\right)}_{u^\star(s,n,t)}. \tag{5.5}$$

Substituting (5.5) yields

$$\mathcal{Q} = -\partial_i \partial_j (U_i^{(sk)} U_j^{(sk)}) - 2\,\partial_i \partial_j \left(U_i^{(sk)} u_j^\star\right) - \partial_i \partial_j \left(u_i^\star u_j^\star\right). \tag{5.6}$$

Because $U^{(sk)}$ has only an s component depending on n, $\partial_i \partial_j (U_i^{(sk)} U_j^{(sk)}) = 0$. The residual product $u_i^\star u_j^\star$ in the last term is volumetric and turbulent throughout the UMZ interior, with no preferred along-plane coherence length, so its wall-parallel spectrum is broadband with substantial content at high (k_x, k_z); under the elliptic Green's mapping, this high-k content is exponentially attenuated before reaching the wall. The cross-term simplifies to

$$-2\,\partial_x \partial_y \left(U^{(sk)} v^{(f)}\right) = -2\,\partial_x \left[(\partial_y U^{(sk)})\, v^{(f)} + U^{(sk)}\, \partial_y v^{(f)}\right]. \tag{5.7}$$

https://doi.org/10.1017/jfm.2026.12040 Published online by Cambridge University Press

In the fissure neighbourhood, $\delta^{(f)} \ll \ell_{s,t}$, so $\partial_n \gg \partial_{s,t}$ and the first product, proportional to $\partial_y U^{(sk)} \sim u_\tau/\delta^{(f)}$, dominates. Thus,

$$\mathcal{Q}^{(f)} \approx -\,2\,\partial_x\partial_y\big(U^{(sk)}\,v^{(f)}\big) \tag{5.8}$$

is compactly supported on the fissure. Integrating across the $O(\delta^{(f)})$ thickness yields the fissure-source density

$$\int \mathcal{Q}^{(f)}\,\mathrm{d}y \approx -2\partial_x[\![U^{(sk)}v^{(f)}]\!], \qquad [\![\cdot]\!] \equiv \text{jump across the fissure.} \tag{5.9}$$

The spectral content of $\mathcal{Q}^{(f)}$ is therefore set by the along-fissure variations of the flux $U^{(sk)}v^{(f)}$, whose scales are $O(\ell_{s,t}) \gg \delta^{(f)}$, so the resulting wall-parallel content sits at low k.

For the linear source, $\partial_n U_s \neq 0$ only within the fissure. Thus,

$$\mathcal{L}^{(f)} = -\,2\,(\partial_n U)\,\partial_s v^{(f)} \approx -\,2\,(\partial_y U)\,\partial_x v^{(f)} \tag{5.10}$$

is likewise localised by $\partial_n U$, with its spectrum set by the along-fissure gradients $\partial_s v^{(f)}$ (low k). In short, both $\mathcal{Q}^{(f)}$ and $\mathcal{L}^{(f)}$ are fissure supported and streamwise biased in wavenumber.

Because the skeletal shear $\partial_y U^{(sk)}$ is not directly accessible from instantaneous fields, we adopt the instantaneous wall-normal shear $\partial_y u$ as a direct operational proxy, and define the fissure support via a soft threshold χ_f applied to $|\partial_y u|$. Substituting $(\partial_y u)_f = \chi_f\,\partial_y u$ for $\partial_n U$ in (5.8)–(5.10) yields the source proxies shown in figure 7. Across this snapshot, 69 % of $|\mathcal{Q}^{(f)}|$ and 91 % of $|\mathcal{L}^{(f)}|$ lie within the identified fissure support, confirming that the retained sources are localised on the high-shear skeleton rather than distributed through the surrounding uniform-momentum interiors.

Finally, the wall imprint of these compact sources is dictated by the elliptic Green's function. Because the wall-parallel Green's weight decays approximately as $e^{-k\,y}$, the broadband wall-parallel content of UMZ-interior fluctuations is strongly filtered, whereas the fissure source – although thin in y – projects onto *low* wall-parallel wavenumbers because of its large along-fissure extent ($\ell_{s,t} \gg \delta^{(f)}$) and therefore transmits efficiently to the wall. This picture is consistent with the UMZ–vortical-fissure structure in which $\Delta U = O(u_\tau)$ across fissures of thickness $\delta^{(f)+} \sim (\delta^+)^{1/2}$ (Klewicki 2013; Bautista *et al.* 2019).

6. Estimate of $A_{\mathcal{Q}}$

We now use the fissure-supported nonlinear source and the elliptic mapping to obtain an order-of-magnitude estimate for the prefactor $A_{\mathcal{Q}}$ in (1.1). From (5.9), a thin fissure at height y supplies a sheet-integrated nonlinear source. Across the inertial region the streamwise velocity jump satisfies $\Delta U = O(u_\tau)$, and we write $\Delta U^+ \equiv \Delta U/u_\tau$. We denote the inertial-layer r.m.s. of v^+ by v^+_{rms}. Approximating $\partial_x v^{(f)} \sim v_{rms}/\ell_s$, with ℓ_s an along-fissure correlation length, the sheet source density scales as

$$\int \mathcal{Q}^{(f)}\,\mathrm{d}y \sim \frac{2\Delta U\; v_{rms}}{\ell_s}\,. \tag{6.1}$$

In the log region, attached-eddy arguments (Townsend 1951) and the UMZ–vortical-fissure picture suggest that the relevant wall-parallel scales grow linearly with y. Following Wei *et al.* (2005) and Klewicki (2021), we write the typical layer width as $W(y) = y/\phi_c$,

https://doi.org/10.1017/jfm.2026.12040 Published online by Cambridge University Press

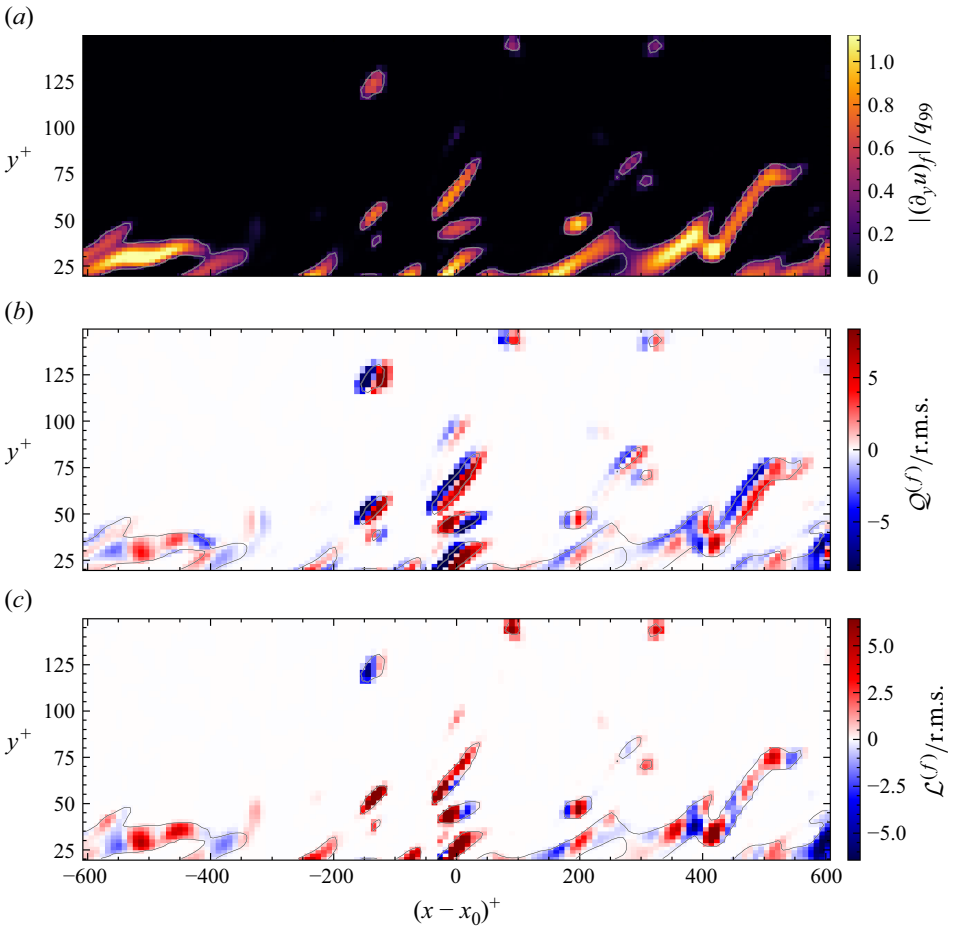


Figure 7. Instantaneous x–y snapshot of the fissure-supported source proxies, with $\partial_y u$ used as a direct proxy for the skeletal shear $\partial_y U^{(sk)}$ (see text). (*a*) Thresholded shear indicator $|(\partial_y u)_f|/q_{99}$, with $(\partial_y u)_f = \chi_f\, \partial_y u$, χ_f a soft (tanh) threshold defining the fissure support, and q_{99} the 99th percentile of $|\partial_y u|$ over the analysed wall-normal band (robust colour-bar scale). (*b*) Nonlinear proxy $\mathcal{Q}^{(f)} = -2\partial_x[(\partial_y u)_f\, v]$ and (*c*) linear proxy $\mathcal{L}^{(f)} = -2(\partial_y u)_f\, \partial_x v$, each normalised by its r.m.s. Contours in (*b*, *c*) repeat the thresholded fissure support.

with the Fife similarity parameter $\phi_c \approx 1.62$. Then taking

$$\ell_s(y) = \alpha W(y) = \alpha \frac{y}{\phi_c}, \tag{6.2}$$

where $\alpha = O(1)$ measures the ratio of along-fissure correlation length to UMZ width. The segment-length statistics of large-scale UMZ interfaces in Cui & Jacobi (2025) show that the wavy segments that compose strongly linear edges have a characteristic length of order $0.1h$ over a wide range of streamwise extents, while the reanalysis of UMZ thicknesses in Heisel *et al.* (2020) and Cui & Jacobi (2025) confirms that $H(y) \sim y$ throughout the logarithmic region. Together, these results support an $O(1)$ ratio $\ell_s/W(y)$ and hence $\alpha = O(1)$. In inner units this gives $y^+/\ell_s^+ = \phi_c/\alpha$, independent of y^+ over the inertial layer.

The wall kernel behaves as $G \sim -k^{-1}\mathrm{e}^{-ky}$ for $k \gg 1$ (see (2.9)). The attribution maps in figure 3 and the envelope in (3.3) indicate that the dominant contribution to the wall

https://doi.org/10.1017/jfm.2026.12040 Published online by Cambridge University Press

pressure from a layer at y comes from wall-parallel wavenumbers satisfying $ky \approx 1$. Evaluating the kernel on this line gives a factor $y\,\mathrm{e}^{-1}$. Combining this with the sheet source scaling yields a single-fissure contribution in inner units

$$p^{(1)+} \sim C_{\mathcal{Q}}^{1/2}\left(2\Delta U^{+} v_{rms}^{+}\right)\mathrm{e}^{-1}\frac{y^{+}}{\ell_{s}^{+}}\,, \tag{6.3}$$

where $C_{\mathcal{Q}} = O(1)$ collects kernel prefactors, the modest anisotropy of the fissure-aligned source and weak bandwidth effects associated with the $ky \simeq 1$ envelope. Using $y^{+}/\ell_{s}^{+} = \phi_c/\alpha$ then gives a single-layer variance

$$\left\langle (p^{(1)+})^2 \right\rangle = C_{\mathcal{Q}}\left(2\Delta U^{+} v_{rms}^{+}\right)^2 \mathrm{e}^{-2}\left(\frac{\phi_c}{\alpha}\right)^2 . \tag{6.4}$$

In the UMZ–fissure hierarchy, the characteristic layer positions satisfy $y_{i+1} = \phi_c y_i$, so the number of inertial-layer levels from $y^{+} \approx \sqrt{\delta^{+}}$ up to $y^{+} \approx \delta^{+}/2$ is

$$N(\delta^{+}) \approx \frac{1}{2\ln\phi_c}\,\ln\delta^{+}\,. \tag{6.5}$$

Assuming that correlations between distinct layers are weak, the nonlinear contribution to the wall-pressure variance may be written as

$$\langle p^{+2}\rangle_{\mathcal{Q}} \approx B_{\mathcal{Q}} + N(\delta^{+})\left\langle (p^{(1)+})^2 \right\rangle, \tag{6.6}$$

so that

$$A_{\mathcal{Q}} = \frac{C_{\mathcal{Q}}}{2\ln\phi_c}\left(2\Delta U^{+} v_{rms}^{+}\frac{\phi_c}{\alpha}\mathrm{e}^{-1}\right)^2 . \tag{6.7}$$

It is convenient to factor out the purely geometrical numerical prefactor associated with the inertial-layer hierarchy. Writing (6.7) as

$$A_{\mathcal{Q}} = C_{\mathcal{Q}}\,\mathcal{M}(\phi_c)\left(\frac{\Delta U^{+} v_{rms}^{+}}{\alpha}\right)^2 , \tag{6.8}$$

we define

$$\mathcal{M}(\phi_c) = \frac{2\phi_c^2}{\ln\phi_c}\,\mathrm{e}^{-2}\,. \tag{6.9}$$

For the Fife similarity parameter $\phi_c \approx 1.62$, this gives $\mathcal{M}(\phi_c) \approx 1.47$, so that the remaining sensitivity of $A_{\mathcal{Q}}$ is contained entirely in the factors ΔU^{+}, v_{rms}^{+}, α and $C_{\mathcal{Q}}$.

Measurements of the velocity jump across UMZ interfaces in high-Re BL particle image velocimetry and DNS show $\Delta U^{+} = O(1)$ and typically slightly greater than unity. The UMZ/VF model of Bautista *et al.* (2019) and the mean-vorticity analysis of Klewicki (2013) both indicate that ΔU scales on u_τ with a range of $\Delta U^{+} \in [1, 1.6]$ and $\langle \Delta U^{+}\rangle \gtrsim 1$ (Bautista *et al.* 2019), while the interface study of De Silva *et al.* (2017) finds velocity jumps concentrated in the range $\Delta U^{+} \in [1, 2]$. DNS channel flow (Hoyas & Jiménez 2006) up to $\delta^{+} \approx 2,000$ likewise show that the inertial-layer wall-normal r.m.s. velocity satisfies $v_{rms}^{+} = O(1)$, with representative values $v_{rms}^{+} \sim [0.9, 1.1]$. Taken together, these results motivate using a central estimate $\Delta U^{+} \approx 1.1$ and $v_{rms}^{+} \approx 1$ for order-of-magnitude purposes.

The segment-length and spacing statistics of Cui & Jacobi (2025) further support an $O(1)$ ratio of along-edge coherence length to UMZ thickness, so for the estimate below we take $\alpha \approx 1$. Finally, $C_{\mathcal{Q}}$ encapsulates the modest spread of Green's function kernel

https://doi.org/10.1017/jfm.2026.12040 Published online by Cambridge University Press

weights, bandwidth and anisotropy about the idealised $ky \simeq 1$ line; in the absence of any strong bias we likewise treat it as an $O(1)$ factor.

Using the central values $\Delta U^+ \approx 1.1$, $v^+_{rms} \approx 1$, $\alpha \approx 1$ and $C_{\mathcal{Q}} \approx 1$ in (6.7) yields

$$A_{\mathcal{Q}} \approx 2\,. \tag{6.10}$$

If instead we let ΔU^+ and v^+_{rms} range over the empirical values quoted above, (6.7) gives a broader, but still order-one, prediction,

$$1.2 \lesssim A_{\mathcal{Q}} \lesssim 4.6\,. \tag{6.11}$$

Thus, the fissure-based picture combined with wall distance scaling robustly produces an $A_{\mathcal{Q}}$ of order unity, consistent with the logarithmic growth of $\langle p^{+2}\rangle$ inferred from figure 1(*b*).

7. Discussion and consequences

These results link the source terms of the pressure Poisson equations to physical processes that enable us to clarify the δ^+ scaling of $\langle p^{+2}\rangle$. We start by introducing the variance attribution map that elucidates the $\xi = O(1)$ attenuation of structures for $k \gtrsim 10$. We then look at the energetic structure of the sources, showing that $\mathcal{L}$ is concentrated in the buffer layer, while $\mathcal{Q}$ is most energetic in the inertial layer. $\mathcal{Q} = \overline{\mathcal{Q}} + \mathcal{T} - \mathcal{S}$ is the difference of two large, strongly correlated quadratic forms; their partial cancellation is central to how $\mathcal{Q}$ maps to the wall. Next, we show that $\mathcal{L}$ is linked to the near-wall process that subsequently provides an $O(1)$ offset to the observed $\langle p^{+2}\rangle(\delta^+)$ growth. Finally, we show that fissures separating UMZs in the inertial layer act as compact carriers of these source terms. However, the detailed evidence assembled here comes from a single channel-flow case at $\delta^+ \approx 550$, so the manuscript cannot by itself establish how broadly the inferred source split generalises across δ^+ or flow configuration.

The conceptual link between the source terms and processes in the turbulent BL allows us to infer scalings for the sources and, via consideration of the Green's function weighting, $\langle p^{+2}\rangle(\delta^+)$. The fissure thickness, when scaled by outer length, decreases approximately as $1/\sqrt{\delta^+}$ while the streamwise velocity jump across a fissure is $O(u_\tau)$. Furthermore, the number of fissures increases approximately as $\ln \delta^+$ (Bautista *et al.* 2019), and the fraction of total vorticity contained in the fissures increases with δ^+ (Klewicki 2013). The fissure thickness sets the scale for the normal gradients in (5.8)–(5.10), while the velocity jump sets the scale for $U^{(sk)}$. The increasing number of fissures and their increasing proportion of total vorticity content with δ^+ imply that the amplitude and intermittency of $\mathcal{Q}$ increase with δ^+, while $\mathcal{L}$ remains approximately constant as it is tied to near-wall processes. Therefore, considering the observed form of the wall-pressure-variance scaling,

$$\langle p^{+2}\rangle = B_{\mathcal{L}} + A_{\mathcal{Q}} \ln \delta^+\,, \tag{7.1}$$

we identify $B_{\mathcal{L}}$ as the asymptotically δ^+-independent offset from $\mathcal{L}$ and $A_{\mathcal{Q}} \ln \delta^+$ as the δ^+-dependent contribution from $\mathcal{Q}$. $A_{\mathcal{Q}} \ln \delta^+$ is therefore tied to the fissure statistics and their evolution with δ^+. That interpretation should nevertheless be viewed as provisional: with only one Reynolds number analysed directly, the present manuscript supports the plausibility of this decomposition but does not uniquely determine the rate at which the coefficients approach their asymptotic forms, nor does it rule out subleading corrections that could matter over a δ^+ range. Even so, the current dataset is already rich enough to show the source localisation and wall-mapping signatures that motivate the proposed decomposition. Finally, we provide an order-of-magnitude estimate of $A_{\mathcal{Q}}$ based on the

https://doi.org/10.1017/jfm.2026.12040 Published online by Cambridge University Press

fissure picture that yields a value consistent with observations. The estimate is sensitive to the choice of parameters, and work to refine these choices would be valuable.

This picture of the mechanisms driving the source terms augments the two-component inner- and outer-spectral nature of the premultiplied wall-pressure spectrum identified by Massey *et al.* (2026*b*): the explicit link to the source-based view is a subject of ongoing work. The working hypothesis universal inner function (their g_1) arises from the near-wall contribution, and the break frequency is defined as the frequency/length scale where the buffer layer contribution is at its maximum. The present variance analysis should not be interpreted as a prediction of the Reynolds-number evolution of the inner spectral peak itself; resolving that question would require source-decomposed k_x–k_z–ω spectra over δ^+. The outer function (their g_2) arises from the inertial layer contribution with the break frequency associated with length scales on the scale of the BL thickness (consistent with inertial layer structures). The present framework provides a spatial description of the mechanisms contributing to $\langle p^{+2}\rangle$ and lays the foundations to understand the spatial contribution to the full 2-D wavenumber frequency map of the pressure fluctuations.

For control and design, where to act follows from the source split. Targeting the inertial layer to weaken intensity or intermittency reduces $A_{\mathcal{Q}}$, while targeting the buffer layer primarily modifies $\mathcal{L}$ and therefore the offset $B_{\mathcal{L}}$. Because $\xi = O(1)$, actuation localised at y_a imprints most strongly near $k \sim O(1)/y_a$, offering a direct spectral target for feedback or open-loop strategies aimed at the most relevant per-decade inertial layer contribution.

The present source split is closely related to the classical vorticity/strain form of the Poisson equation proposed by Bradshaw & Koh (1981) and discussed by Adrian (1982), who stressed that any such decomposition is algebraically non-unique and that the physically important distinction is between local, irrotational pressure and the non-local rotational contribution. Recasting the equation in terms of $\mathcal{L}$ and $\mathcal{Q}$ shows that this 'rotational' pressure is, in practice, carried by compact vortical fissures in the inertial region, consistent with the vorticity-centric descriptions of Klewicki (2013), Morrill-Winter & Klewicki (2013) and the UMZ-fissure model of Bautista *et al.* (2019). Combined with the elliptic Green's weighting identified in earlier DNS studies (Kim 1989; Chang *et al.* 1999; Anantharamu & Mahesh 2020), this picture explains how a δ^+-independent near-wall contribution from $\mathcal{L}$ supplies the offset $B_{\mathcal{L}}$, while the hierarchy of fissure-supported $\mathcal{Q}$ sources yields the $A_{\mathcal{Q}} \ln \delta^+$ growth of $\langle p^{+2}\rangle$, thereby providing a mechanistic underpinning for the matched-asymptotic description of wall-pressure variance (Panton *et al.* 2017).

In summary, this conceptual picture maps the interface between UMZs in turbulent BLs to the spectral content of wall pressure and provides a compact lever for models, diagnostics and control. By tracing how sheet-like structures feed the nonlinear Poisson source and are transmitted to the wall through a radially weighted Green's mapping, this framework connects wall-pressure behaviour to a vorticity-centric description of inertial layer dynamics (Klewicki 2013) and supplies a mechanistic rationale for the logarithmic growth highlighted by matched-asymptotic theory (Panton *et al.* 2017). Its quantitative generality, however, remains to be tested by repeating the source decomposition and attribution analysis over a wider range of δ^+ and, ideally, across multiple wall-bounded flow geometries. The present $\delta^+ \approx 550$ case should therefore be viewed as an illustrative proof of mechanism rather than as a final test of universality.

Acknowledgements. The authors thank an anonymous referee for the suggestion that led to figure 7, which directly visualises the compact support of the linear and nonlinear sources on the vortical fissure skeleton and meaningfully strengthens the mechanistic story.

https://doi.org/10.1017/jfm.2026.12040 Published online by Cambridge University Press

Funding. The support from DARPA under award HR0011-24-9-0465 and the support of ONR to CTR under grant N000142312833 is gratefully acknowledged.

Declaration of interests. The authors report no conflict of interest.

Data availability statement. The data that support the findings of this study will be made available upon request.

References

ADRIAN, R.J. 1982 Comment on 'A note on Poisson's equation for pressure in a turbulent flow'. *Phys. Fluids* **25** (3), 577–577.

ANANTHARAMU, S. & MAHESH, K. 2020 Analysis of wall-pressure fluctuation sources from direct numerical simulation of turbulent channel flow. *J. Fluid Mech.* **898**, A17.

BAUTISTA, J.C.C., EBADI, A., WHITE, C.M., CHINI, G.P. & KLEWICKI, J.C. 2019 A uniform momentum zone-vortical fissure model of the turbulent boundary layer. *J. Fluid Mech.* **858**, 609–633.

BLANCO, D.C.P., HANIFI, A., HENNINGSON, D.S. & CAVALIERI, A.V.G. 2024 Linear and nonlinear receptivity mechanisms in boundary layers subject to free-stream turbulence. *J. Fluid Mech.* **979**, A31.

BRADSHAW, P. 1967 'Inactive' motion and pressure fluctuations in turbulent boundary layers. *J. Fluid Mech.* **30**, 241–258.

BRADSHAW, P. & KOH, Y.M. 1981 A note on Poisson's equation for pressure in a turbulent flow. *Phys. Fluids* **24** (4), 777–777.

CHANG, P.A., PIOMELLI, U. & BLAKE, W.K. 1999 Relationship between wall pressure and velocity-field sources. *Phys. Fluids* **11**, 3434–3448.

CHEN, X. & SREENIVASAN, K.R. 2023 Reynolds number asymptotics of wall-turbulence fluctuations. *J. Fluid Mech.* **976**, A21.

CHOI, H. & MOIN, P. 1990 On the space-time characteristics of wall-pressure fluctuations. *Phys. Fluids A* **2**, 1450–1460.

CUI, G. & JACOBI, I. 2025 Geometry of large-scale uniform momentum zone interfaces. *J. Fluid Mech.* **1024**, A35.

DACOME, G., LAZZARINI, L., TALAMELLI, A., BELLANI, G. & BAARS, W.J. 2025 Scaling of wall-pressure-velocity correlations in high-Reynolds-number turbulent pipe flow. *J. Fluid Mech.* **1013**, A48.

DE, S., CHARITHA, M., PHILIP, J., HUTCHINS, N. & MARUSIC, I. 2017 Interfaces of uniform momentum zones in turbulent boundary layers. *J. Fluid Mech.* **820**, 451–478.

DESHPANDE, R., HASSANEIN, A. & BAARS, W.J. 2026 Convection velocities and velocity coupling of outer-scaled wall-pressure fluctuations in canonical turbulent boundary layers. *Phys. Rev. Fluids* **11** (6), 064612.

DESHPANDE, R., VINUESA, R., KLEWICKI, J. & MARUSIC, I. 2025 Active and inactive contributions to the wall pressure and wall-shear stress in turbulent boundary layers. *J. Fluid Mech.* **1003**, A24.

FARABEE, T.M. & CASARELLA, M.J. 1991 Spectral features of wall pressure fluctuations beneath turbulent boundary layers. *Phys. Fluids A* **3**, 2410–2420.

FLORES, O. & JIMÉNEZ, J. 2006 Effect of wall-boundary disturbances on turbulent channel flows. *J. Fluid Mech.* **566**, 357–376.

FRITSCH, D., VISHWANATHAN, V., DUETSCH-PATEL, J., GARGIULO, A., LOWE, K.T. & DEVENPORT, W.J. 2020 The pressure signature of high Reynolds number smooth wall turbulent boundary layers in pressure gradient family. In *AIAA Aviation 2020 Forum*, p. 3066. AIAA.

FRITSCH, D.J., VISHWANATHAN, V., TODD LOWE, K. & DEVENPORT, W.J. 2022 Fluctuating pressure beneath smooth wall boundary layers in nonequilibrium pressure gradients. *AIAA J.* **60**, 4725–4743.

GEROLYMOS, G.A., SÉNÉCHAL, D. & VALLET, I. 2013 Wall effects on pressure fluctuations in turbulent channel flow. *J. Fluid Mech.* **720**, 15–65.

GIBEAU, B. & GHAEMI, S. 2021 Low- and mid-frequency wall-pressure sources in a turbulent boundary layer. *J. Fluid Mech.* **918**, A18.

HEISEL, M., DE SILVA, C.M., HUTCHINS, N., MARUSIC, I., GUALA, M. 2020 On the mixing length eddies and logarithmic mean velocity profile in wall turbulence. *J. Fluid Mech.* **887**, R1.

HEISEL, M., DE SILVA, C.M., KATUL, G.G., CHAMECKI, M. 2022 Self-similar geometries within the inertial subrange of scales in boundary layer turbulence. *J. Fluid Mech.* **942**, A33.

HOYAS, S. & JIMÉNEZ, J. 2006 Scaling of the velocity fluctuations in turbulent channels up to $\mathrm{Re} = 2003$. *Phys. Fluids* **18**, 011702.

HOYAS, S., OBERLACK, M., ALCÁNTARA-ÁVILA, F., KRAHEBERGER, S.V., LAUX, J. 2022 Wall turbulence at high friction Reynolds numbers. *Phys. Rev. Fluids* **7** (1), 014602.

https://doi.org/10.1017/jfm.2026.12040 Published online by Cambridge University Press

HU, Z.W., MORFEY, C.L. & SANDHAM, N.D. 2006 Wall pressure and shear stress spectra from direct simulations of channel flow. *AIAA J.* **44**, 1541–1549.

HUANG, Y., TOEDTLI, S.S., CHINI, G.P. & MCKEON, B.J. 2026 Spatio-temporal characterization of nonlinear forcing and response in turbulent channel flow. *J. Fluid Mech.* **10**, A37.

JIMENEZ, J. & HOYAS, S. 2008 Turbulent fluctuations above the buffer layer of wall-bounded flows. *J. Fluid Mech.* **611**, 215–236.

KIM, J. 1989 On the structure of pressure fluctuations in simulated turbulent channel flow. *J. Fluid Mech.* **205**, 421.

KLEWICKI, J.C. 2013 A description of turbulent wall-flow vorticity consistent with mean dynamics. *J. Fluid Mech.* **737**, 176–204.

KLEWICKI, J.C. 2021 Properties of turbulent channel flow similarity solutions. *J. Fluid Mech.* **915**, A39.

KLEWICKI, J.C., PRIYADARSHANA, P.J.A. & METZGER, M.M. 2008 Statistical structure of the fluctuating wall pressure and its in-plane gradients at high Reynolds number. *J. Fluid Mech.* **609**, 195–220.

LEE, M. & MOSER, R.D. 2015 Direct numerical simulation of turbulent channel flow up to. *J. Fluid Mech.* **774**, 395–415.

MANSOUR, N.N., KIM, J. & MOIN, P. 1988 Reynolds-stress and dissipation-rate budgets in a turbulent channel flow. *J. Fluid Mech.* **194**, 15–44.

MASSEY, J.M.O., SMITS, A.J. & MCKEON, B.J. 2026*b* Two-component inner–outer scaling model for the wall-pressure spectrum at high Reynolds num*b*er. *J. Fluid Mech.* **1034**, A60.

MASSEY, J.M.O., ZIMMERMAN, S.J., KLEWICKI, J.C. & MCKEON, B.J. 2026*a*, An inner-scaled linear contribution to wall-pressure variance at high Reynolds number. arXiv preprint arXiv: 2607.02395.

MCKEON, B.J. & SHARMA, A.S. 2010 A critical-layer framework for turbulent pipe flow. *J. Fluid Mech.* **658**, 336–382.

MEINHART, C.D. & ADRIAN, R.J. 1995 On the existence of uniform momentum zones in a turbulent boundary layer. *Phys. Fluids* **7**, 694–696.

MORRILL-WINTER, C. & KLEWICKI, J. 2013 Influences of boundary layer scale separation on the vorticity transport contribution to turbulent inertia. *Phys. Fluids* **25**, 015108.

NAGIB, H., VINUESA, R. & HOYAS, S. 2024 Utilizing indicator functions with computational data to confirm nature of overlap in normal turbulent stresses: logarithmic or quarter-power. *Phys. Fluids* **36** (7), 075145.

OBERLACK, M., HOYAS, S., KRAHEBERGER, S.V., ALCÁNTARA-ÁVILA, F., LAUX, J. 2022 Turbulence statistics of arbitrary moments of wall-bounded shear flows: a symmetry approach. *Phys. Rev. Lett.* **128** (2), 024502.

PANTON, R.L., LEE, M. & MOSER, R.D. 2017 Correlation of pressure fluctuations in turbulent wall layers. *Phys. Rev. Fluids* **2**, 094604.

PIROZZOLI, S. & WEI, T. 2025 On pressure fluctuations in the near-wall region of turbulent flows. *J. Fluid Mech.* **1010**, A10.

PRIYADARSHANA, P.J.A., KLEWICKI, J.C., TREAT, S. & FOSS, J.F. 2007 Statistical structure of turbulent-boundary-layer velocity-vorticity products at high and low Reynolds numbers. *J. Fluid Mech.* **570**, 307–346.

ROSENBERG, K. & MCKEON, B.J. 2019 Efficient representation of exact coherent states of the Navier–Stokes equations using resolvent analysis. *Fluid Dyn. Res.* **51** (1), 011401.

SCHLATTER, P. & ÖRLÜ, R. 2010 Assessment of direct numerical simulation data of turbulent boundary layers. *J. Fluid Mech.* **659**, 116–126.

TOWNSEND, A.A. 1951 The structure of the turbulent boundary layer. *Math. Proc. Camb. Phil. Soc.* **47** (2), 375–395.

WEI, T., FIFE, P., KLEWICKI, J. & MCMURTRY, P. 2005 Properties of the mean momentum balance in turbulent boundary layer, pipe and channel flows. *J. Fluid Mech.* **522**, 303–327.

YANG, B. & YANG, Z. 2022 On the wavenumber-frequency spectrum of the wall pressure fluctuations in turbulent channel flow. *J. Fluid Mech.* **937**, A39.

https://doi.org/10.1017/jfm.2026.12040 Published online by Cambridge University Press